Chemical Engineering Journal 535 (2026) 175423

Contents lists available at ScienceDirect

Chemical Engineering Journal

journal homepage: www.elsevier.com/locate/cej

Double substituted Co-free perovskite oxides for quasi-symmetric reversible solid oxide cells (rSOCs)

Anna Paola Panunzi [a,c], Leonardo Duranti [a,*], Isabella Natali Sora [b,*], Renato Pelosato [b], Benedetta Bertolotti [b], Umberto Pasqual Laverdura [c], Maria Luisa Grilli [c], Elisabetta Di Bartolomeo [a]

[a] Department of Chemical Science and Technologies, University of Rome Tor Vergata, Via della Ricerca Scientifica, 00133, Rome, Italy
[b] Department of Engineering and Applied Science, University of Bergamo, Dalmine, BG, I-24044, Italy
[c] ENEA, Department of Energy Technologies and Renewable Sources (TERIN), Division of Technologies and Vectors for Decarbonization (DEC), Casaccia Research Centre - Via Anguillarese 301 – 00123, S.M. di Galeria, Rome, Italy

ARTICLE INFO

Keywords:
Perovskite oxides
B-site substitution
SOEC
CO_2 conversion
Symmetric SOC
Reversible solid oxide cell (rSOC)

ABSTRACT

High-temperature CO_2 electrolysis in solid oxide electrochemical cells offers one of the most efficient routes for carbon dioxide conversion, enabling the production of highly pure carbon monoxide due to favorable thermodynamics and fast kinetics above 600 °C. The emergence of CO:CO_2 reversible solid oxide cells (rSOCs) further enhances system efficiency, promoting integration with CO_2-rich and CO-rich industrial exhaust streams. However, reversible operation imposes stringent requirements on electrode materials, which must combine high catalytic activity, redox stability, and long-term durability under a wide range of oxygen partial pressures.

Herein, we report a doubly B-site–substituted perovskite, $La_{0.6}Sr_{0.4}Fe_{0.6}Mn_{0.2}M_{0.2}O_{3-\delta}$ (M = Cu, Ni), as a multifunctional electrode platform for rSOCs. Both $La_{0.6}Sr_{0.4}Fe_{0.6}Mn_{0.2}Cu_{0.2}O_{3-\delta}$ (LSFMC) and $La_{0.6}Sr_{0.4}Fe_{0.6}Mn_{0.2}Ni_{0.2}O_{3-\delta}$ (LSFMN) are synthesized as single-phase perovskites, with rhombohedral symmetry (*R-3c*). When evaluated as oxygen electrodes in symmetric cell configurations, LSFMC and LSFMN exhibit significantly enhanced oxygen electrocatalysis, achieving a decrease in area-specific resistance by 51% and 38%, respectively, compared to the unsubstituted material. Under reducing conditions, LSFMN undergoes controlled and homogeneous exsolution of Fe—Ni nanoparticles, generating catalytically active metallic domains while preserving structural integrity. A quasi-symmetric electrolyte-supported cell based on $La_{0.8}Sr_{0.2}Ga_{0.8}Mg_{0.2}O_{3-\delta}$ (LSGM) electrolyte, employing LSFMN as fuel electrode and LSFMC as air electrode, demonstrates excellent performance and durability in both CO-fuelled solid oxide fuel cell mode and CO_2 electrolysis mode. Stable and reversible operation is maintained for over 150 h in a 50:50 CO:CO_2 mixture.

Targeted B-site substitution of Mn-stabilized ferrites enables the design of high-performance, cobalt-free and reversible electrodes, offering a promising strategy for next-generation rSOCs.

1. Introduction

Among carbon dioxide conversion technologies, high temperature electrolysis via Solid Oxide Electrolyzers (SOECs) stands out for unrivalled efficiency. At temperatures above 600 °C, the theoretical voltage required for CO_2 reduction is lower compared to the same reaction occurring at room temperature, with significantly enhanced reaction kinetics [1]. CO_2-SOECs are currently being commercialized [2] as they allow for the reliable production of highly pure carbon monoxide readily collected in the exhaust lines. CO is a valuable reactant in industrial processes, the Fischer-Tropsch route to hydrocarbons production being the most relevant. Since transition metal-based CO_2-SOEC fuel electrodes can be oxidized when exposed to pure CO_2 at high temperature, a fraction of carbon monoxide is commonly present in the CO_2-SOEC inlet stream as a protecting gas [3]. CO can also be effectively used as fuel for Solid Oxide Fuel Cells (SOFCs), provided that the electrocatalyst and the anodic compartment are designed to withstand and tolerate coking [4]. Recently, the concept of CO:CO_2 reversible solid oxide cells (rSOCs) has witnessed increasing interest as rSOCs would allow for interchangeable operation between CO oxidation and CO_2 reduction, increasing the fuel

* Corresponding authors.
E-mail addresses: leonardo.duranti@uniroma2.it (L. Duranti), isabella.natali-sora@unibg.it (I. Natali Sora).

https://doi.org/10.1016/j.cej.2026.175423
Received 19 January 2026; Received in revised form 18 March 2026; Accepted 19 March 2026
Available online 20 March 2026

cell-electrolyzer round trip efficiency [5,6]. Moreover, rSOCs could be integrated into large-scale manufacturing processes (e.g. cement and steel production) that give off high-temperature CO_2-rich [7] and CO-rich exhausts [8], towards decarbonization. Efforts are currently being directed towards the design of high-performing, long-lasting and possibly critical elements-free electrode materials. Versatility is the main requirement that an rSOC electrode must possess, as on one hand it must be catalytically active for CO oxidation and CO_2 reduction, on the other hand for oxygen reduction reaction (ORR) and oxygen evolution reaction (OER). The reference SOC fuel electrode material is the nickel and yttria-stabilized zirconia (YSZ) cermet. The former, accounting for up to 40–60% of the electrode, provides high electrocatalytic activity both towards CO oxidation and CO_2 reduction, and the latter ensures mechanical support and oxide ions permeation. Besides the long-standing issue related to the likelihood of passivating Ni sites over time due to coking during CO oxidation and carbon deposition during CO_2 reduction, Ni oxidation threatens cell stability as it goes along with large volume variation [9]. This latter aspect represents an issue especially for reversible operation, as the fuel electrode is repeatedly exposed to large pO_2 variations. In the last decade, the catalytically active metal surface segregation in form of evenly distributed nanoparticles via the exsolution phenomenon has become a consolidated strategy to both improve the fuel electrode tolerance against passivation and preserve its mechanical stability upon reoxidation. To cover the oxide surface with evenly distributed exsolved nanoparticles, a minimum amount of catalyst is needed, while its active surface exposure is maximized. This latter aspect allowed for the utilization of limited amounts of platinum group metals, keeping the total catalyst cost comparable to state-of-the-art materials [10–12].

On the other side of the cell, the air electrode material must possess mixed ionic-electronic conductivity and high OER/ORR catalytic activity. $La_{0.6}Sr_{0.4}Fe_{0.8}Co_{0.2}O_{3-\delta}$ and $Ba_{0.5}Sr_{0.5}Co_{0.8}Fe_{0.2}O_{3-\delta}$ show outstanding performance for oxygen electrocatalysis, yet Co-based oxides display too large thermal expansion coefficients for long-term applications in rSOCs [13–15]. Furthermore, Co has been listed as both a critical and a strategic raw material in the European Critical Raw Materials Act [16,17]. Nevertheless, A site Sr-substituted ferrites have been widely investigated as solid oxide cell oxygen electrodes [18], thanks to iron favorable redox chemistry that, besides ensuring suitable electronic conductivity, tolerates replacement to a large extent without leading to lattice collapse. This latter aspect has been recently pushed beyond the stoichiometric limits, tailoring high entropy oxides featuring at least five elements [19], that have proven to be effective as SOFCs cathodes [20,21], SOECs anodes [22] and, in general, as rSOCs oxygen electrodes [13,23,24]. Structural instability prevents the utilization of ferrites at the fuel electrode: in reducing conditions or under large cathodic biases, iron is reduced to its metallic state, leading to a lattice collapse in a mixture of insulating oxides [25,26]. It has been demonstrated that 20 mol% Fe replacement with Mn guides the LSF lattice towards a (reversible) phase transition in reducing conditions to a single Ruddlesden-Popper phase with homogeneously distributed Fe^0 domains that can act as catalytic sites [27]. Mn-substitution allowed for the utilization of LSFM as SOFC anode both in hydrogen [28] and methane [29]. Recently, LSFM has been successfully tested as SOEC electrode for CO_2 electrolysis and CO_2:H_2O co-electrolysis [30,31], and its catalytic activity was further increased via metal additives decoration (Co, Fe, Ni, and Ru) [32], mixing with Fe—Ni powder [33], CeO_2 infiltration [34] or A site substitution [35].

In this work, the effect of a further 20 mol% B-site substitution in $La_{0.6}Sr_{0.4}Fe_{0.8}Mn_{0.2}O_{3-\delta}$ LSFM was explored to enhance electrocatalytic performance at both electrodes. Specifically, $La_{0.6}Sr_{0.4}Fe_{0.6}Mn_{0.2}Cu_{0.2}O_{3-\delta}$ (LSFMC) and $La_{0.6}Sr_{0.4}Fe_{0.6}Mn_{0.2}Ni_{0.2}O_{3-\delta}$ (LSFMN) single phases were synthesized and characterized as air and fuel electrodes, respectively. In symmetric cell tests in air, LSFMC displayed significantly lower area-specific resistance compared to the non-substituted LSFM perovskite, proving to be an ideal candidate for application at the air electrode. Under reducing conditions, a uniform exsolution of Fe—Ni nanoparticles on LSFMN surface significantly enhanced catalytic activity. Quasi-symmetric all-perovskite rSOCs featuring the same stable perovskite oxide backbone (LSFM) at both electrodes, activated by targeted introduction of B-site substitutional Ni at the fuel electrode and Cu at the air electrode, were successfully fabricated and tested. The limited amount of Ni, fully exploited through exsolution, endowed LSFM with long-lasting electrocatalytic activity for CO oxidation/CO_2 reduction. On the other side of the cell, Co-free LSFMC displayed remarkable ORR/OER activity. A proof-of-concept device demonstrated stable operation for over 150 h cycling between CO-SOFC and CO_2-SOEC modes.

2. Experimental

2.1. Perovskite oxides synthesis and reducing treatments

Doped lanthanum ferrites of formula $La_{0.6}Sr_{0.4}Fe_{0.8}Mn_{0.2}O_{3-\delta}$ (LSFM), $La_{0.6}Sr_{0.4}Fe_{0.6}Mn_{0.2}Ni_{0.2}O_{3-\delta}$ (LSFMN) and $La_{0.6}Sr_{0.4}Fe_{0.6}Mn_{0.2}Cu_{0.2}O_{3-\delta}$ (LSFMC) were prepared by auto-combustion of dry gel obtained from a solution of the corresponding nitrates in citric acid solution. Analytical grade La_2O_3, $Sr(NO_3)_2$, $Fe(NO_3)_3{\cdot}9H_2O$, $Mn(NO_3)_2{\cdot}4H_2O$, $Ni(NO_3)_2{\cdot}6H_2O$, $Cu(NO_3)_2{\cdot}2.5H_2O$, citric acid, nitric acid, and aqueous NH_3 were used as starting materials (Sigma-Aldrich). La_2O_3 was weighed after previous thermal treatment at 900 °C for 10 h and dissolved in nitric acid solution. Stoichiometric amounts of metal nitrates were dissolved in water (0.1 $mol{\cdot}L^{-1}$) by stirring on a hotplate and then the solution was poured into the citric acid solution, with the molar ratio of metal ions to citric acid being set at 1:1. During the evaporation process, the precursor solution was neutralized to pH ~ 7 using ammonia solution, promoting the gelation without cation precipitation. The dry gel was heat-treated at 250 °C to start auto-combustion. The resulting ash-like powder was calcined at 600 °C for 6 h in air (5 °C·min^{-1}) to remove any organic residues. 600 °C was observed to be the lowest calcination temperature at which a pure phase of the parent $La_{0.6}Sr_{0.4}FeO_3$ (LSF) was achieved. The introduction of 20 mol% Mn at B site in the perovskite structure of LSF required increasing the calcination temperature to 900 °C, since as reported in our previous study LSFM powder calcined at 850 °C for 5 h revealed the presence of two phases [27]. The powders were thus calcined at 900 °C for 6 h. The final color of the samples was dark grey/black.

As prepared samples underwent a reducing treatment to evaluate the structural and morphological evolution in fuel side conditions. Approximately 50 mg of sample were placed in an alumina crucible and kept at 850 °C for 2 h in flowing 5% H_2/Ar (100 $cm^3{\cdot}min^{-1}$). The reduced materials have been labeled as LSFM_R, LSFMN_R and LSFMC_R. A similar treatment was carried out in a 50:50 CO:CO_2 gas mixture for LSFMN only, to evaluate its structural integrity in CO:CO_2 rSOC fuel side conditions.

2.2. Structural and morphological characterization

Phase purity, lattice symmetry, and unit-cell parameters were determined by powder X-ray diffraction (XRPD). The XRPD patterns were collected using a Bruker D8 Advance powder diffractometer operating in Bragg-Brentano reflection geometry with Cu-Kα radiation and equipped with a LynxEye XE detector. The adopted experimental conditions were a 2θ range 5°-90°, a step size 0.011°, a counting time 19.2 s per step and room temperature. The structural refinements were carried out with the Rietveld method of profile analysis using the program GSAS [36].The refined parameters included scale factor, background function (Chebyshev polynomial), profile parameters (pseudo-Voigt profile function), lattice parameters, atomic coordinates and site occupancy factors of some cations. The occupation factors were fixed considering sample stoichiometry, assuming that all oxygen sites were fully occupied.

Micromeritics Tristar II Plus Surface Area and Pore Size Analyzer was

used to determine the surface areas and pore distributions of as prepared samples. The N_2 adsorption/desorption isotherms were acquired at −196 °C and the surface area was obtained applying the Brunauer-Emmett-Teller method (BET) in a linear 0.03÷0.3 span of relative pressure (p/p_0). All the samples were degassed overnight in vacuum at 350 °C in N_2 flow before analysis.

Thermogravimetric analysis was carried out using a TG-DSC 1 (Mettler Toledo, STAR system). Measurements were performed on ~30 mg of sample in a Pt crucible, pre-treated up to 900 °C in air flux to desorb any contaminants off the sample surface. After cooling to room temperature, the mass loss evaluation was recorded between 50 °C and 900 °C with a heating ramp of 5 °C•min^{-1} in N_2 flux. For each measurement, the buoyancy effect was subtracted.

Temperature programmed reduction in H_2 (H_2-TPR) analysis was performed using an automated flow-through device equipped with a TCD detector (AutoChem 2950 HP Micromeritics), flowing 30 cm^3·min^{-1} of 5% H_2/Ar gas mixture in the reactor, between 50 °C and 900 °C (10 °C•min^{-1}). The H_2 consumption was recorded by a TCD detector and CuO (99.99%, Aldrich®) was reduced for TCD calibration.

A field emission scanning electron (FE-SEM) microscope Carl Zeiss SUPRA™ 35 FE-SEM was used to perform the morphological analysis on as prepared and reduced samples. The elemental distribution was obtained with a field emission scanning electron microscope TESCAN CLARA 2 UHR FE-SEM equipped with an Energy-dispersive X-ray Spectroscopy apparatus (EDX) SDD detector AZtec Ultim® Max ("Infinity") 170 mm^2 by Oxford Instruments.

Transmission Electron Microscopy (TEM) study was carried out with a FEI Tecnai G2 F20 transmission electron microscope operating with a field emission gun (FEG) at an accelerating voltage of 200 kV. The instrument features S-Twin pole pieces with a point-to-point resolution of 0.24 nm. An energy-dispersive X-ray spectrometer (EDS) with an ultrathin window was employed for elemental analysis. Image acquisition was performed using a Gatan TV-rate 626 detector and a Gatan slow-scan CCD model 974. For the analysis, a small amount of each powder was dispersed in isopropyl alcohol, and a drop of the resulting suspension was deposited onto carbon-coated copper or gold grids.

2.3. Cell architecture

All the electrochemical measurements were carried out on electrolyte-supported cells. The solid electrolyte was obtained by mixing $La_{0.8}Sr_{0.2}Ga_{0.8}Mg_{0.2}O_{3-\delta}$ (LSGM, purchased by *Praxair*) with 5 wt% of polyvinylpyrrolidone (PVP), pressed at 370 MPa and sintered at 1500 °C, 2 °C •min^{-1} for 10 h. The final dense pellets show 10 mm diameter and ~ 200 μm thickness, with a relative density of 96%.

An ink was obtained by mixing the selected perovskite powder with serigraphic terpineol-based oil (purchased by *Fuelcellmaterials*). Spin-coating was used at the fuel side, while the air electrode was deposited on the other side by paint-brushing. After deposition, the cell was fired 2 h at 1100 °C, 5 °C•min^{-1} to promote the electrode/electrolyte adhesion. Gold paste (T10112, Metalor Technologies Ltd., U.K.) and gold wires (Au 99.99%) were used as current collectors.

2.4. Electrochemical characterization

Electrochemical Impedance Spectroscopy (EIS) was used to determine area-specific resistance (ASR) on symmetric cells. A frequency response analyzer (FRA, Solartron 1260) coupled with a dielectric interface (Solartron 1296) were used to perform the measurements, with 10 mV AC voltage amplitude in the 0.01 Hz-2 MHz frequency range. ASR vs temperature was evaluated in the 550 °C–850 °C range, in air flux (0.21 atm of O_2). EIS analysis on symmetric cells was used to evaluate the electrode polarization resistance in different conditions: at fixed temperature (750 °C) varying pO_2 (0.01 atm-0.21 atm); at fixed temperature (850 °C) in 50:50 CO:CO_2 atmosphere; at fixed temperature (850 °C) in CO_2 atmosphere both at open circuit voltage and under applied 1.2 V DC bias. The distribution of relaxation times (DRT) analysis was used to investigate the different processes occurring at the electrode. A MATLAB tool developed by Ciucci et al. was used [37].

The complete cell tests were performed on a lab-scale station, where the cell was mounted and sealed with commercial ceramic paste (Aremco Ceramabond 552). All the electrochemical characterization were recorded with a PARSTAT 2273 potentiostat-galvanostat/EIS analyzer. Each test was carried out with the same routine, starting from H_2-SOFC, CO_2-SOEC and reversible SOC in 50:50 CO:CO_2 gas mixture. Each measurement was carried out at 850 °C, with the air side exposed to static air and the fuel side exposed to constant flux of 100 cm^3•min^{-1} of the inlet gas, depending on the tests (pure H_2, pure CO_2 and 50:50 CO:CO_2).

3. Results and discussion

3.1. Structural and morphological analysis of as prepared compounds

Fig. 1a shows the XRPD patterns of the as prepared LSFM, LSFMN and LSFMC samples. All the samples exhibit a single phase corresponding to $La_{0.6}Sr_{0.4}Fe_{0.8}Mn_{0.2}O_{3-\delta}$. An enlargement of the most intense peak reveals a systematic shift towards higher 2θ angles for the Ni- and Cu-substituted samples, from 2θ = 32.56° of LSFM to 32.61° for LSFMN and 32.62° for LSFMC. This shift indicates the effective incorporation of 20 mol% Cu and Ni through substitution of Fe at the B-site.

The Rietveld refinements have been carried out for all samples, and the results are shown in Fig. 1b, c, d, while the refined lattice parameters are reported in Table 1. The structures of all compounds were refined assuming the space group *R-3c* and the atomic configuration described in ref. [38] for $La_{0.6}Sr_{0.4}FeO_{3-\delta}$. The refinement of LSFM proceeded steadily (R_{Bragg} = 2.07, reduced χ^2 = 2.03) and the refined lattice parameters are in good agreement with values reported in previous literature [28]. In contrast, LSFMC and LSFMN were more challenging to refine (R_{Bragg} = 4.26, reduced χ^2 = 2.30 for LSFMN, and R_{Bragg} = 4.27, reduced χ^2 = 2.83 for LSFMC). Refinement assuming orthorhombic symmetry (space group *Pnma*) did not result in a significant improvement of the refinement indexes. For LSFMN and LSFMC the close similarity of the refinement indexes is likely related to the fact that the parent LSFM is on the border of the phase transition from rhombohedral to orthorhombic structure. The normalized volume V_n, calculated as the cell volume V divided by the number of formula units in the unit cell (Z), is smaller for LSFMN and LSFMC than LSFM. Since the ratio between lanthanum and strontium on the A-site is constant, the V_n decrement is likely due to the contraction of B-site coordination polyhedron consequent to the oxidation of the transition metal ions.

The B-site substitution effects on the perovskite oxide morphology were assessed by SEM and TEM. Compared to LSFM microstructure shown in Fig. 2a, the introduction of 20 mol% of Ni in the structure does not lead to any substantial morphological changes (Fig. 2d). In contrast LSFMC exhibits an agglomeration of the oxide particles, resulting in a more compact structure (Fig. 2g). The TEM micrographs in Fig. 2b, e, h confirm what was already observed via SEM, revealing loosely packed aggregates of nanoparticles with irregular morphology and well-defined crystalline facets for LSFM and LSFMN. The average particle diameter is on the order of a few tens of nanometres, while LSFMC exhibits a more densely consolidated structure with larger crystallites, indicative of enhanced grain growth and sintering. High resolution TEM micrographs in Fig. 2c, f, i show *d*-spacing values compatible with those obtained from Rietveld refinement of the rhombohedral *R-3c* perovskite structures: *d* = 0.233 nm *(201)* for LSFM; *d* = 0.274 nm *(104)* for LSFMN and LSFMC.

To complete the structural and morphological characterization of the as prepared materials, the BET surface areas and pore distributions were assessed, and the results are presented in Figs. 2l and S1. The LSFMC sample exhibits a surface area of 4.61 m^2·g^{-1}, which is approximately one-third of that observed for LSFMN (11.62 m^2·g^{-1}) and LSFM (12.06

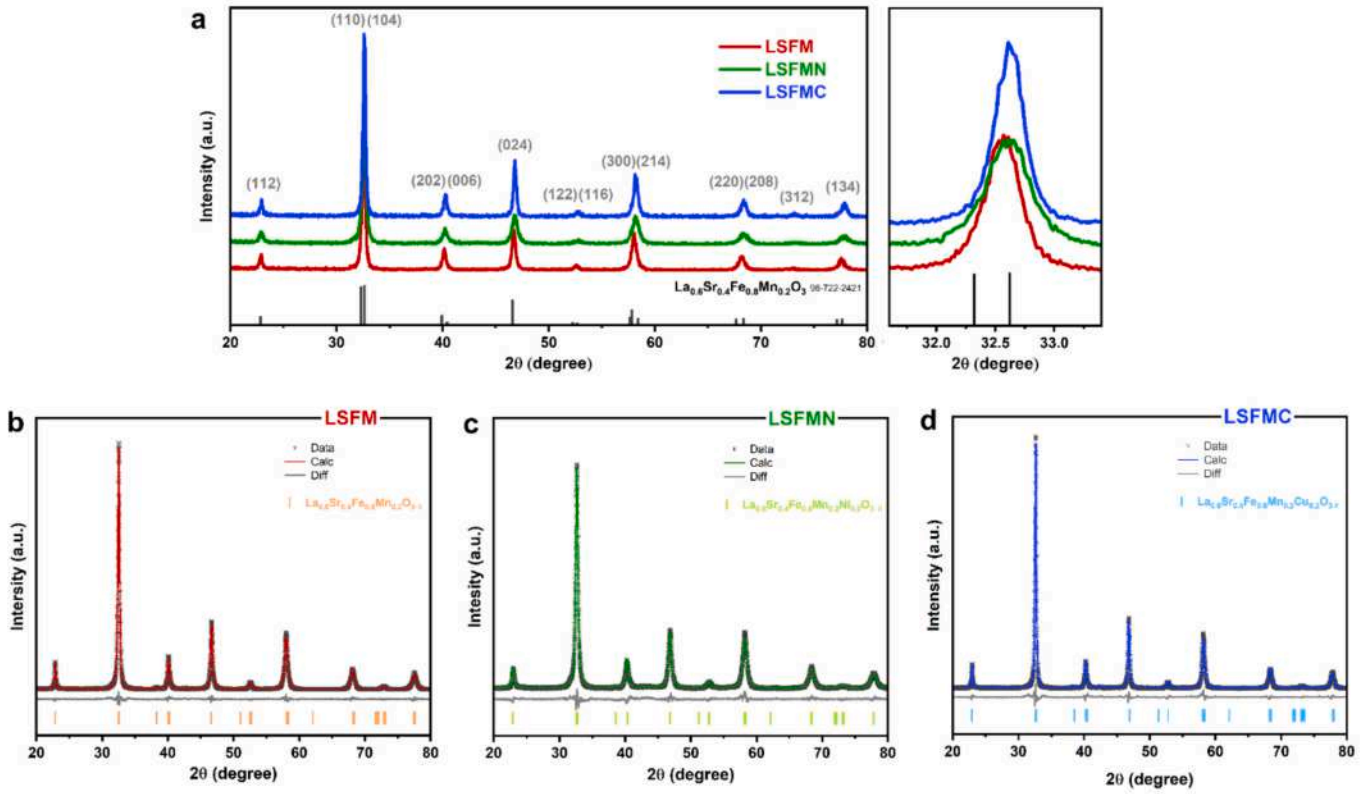

Fig. 1. Structural characterization of as prepared materials: a) XRPD patterns comparison of LSFM, LSFMN and LSFMC, with an enlargement around the most intense peak at 2θ = 32.6°; Rietveld refinement of b) LSFM, c) LSFMN and d) LSFMC.

Table 1
Crystal data obtained by Rietveld refinement using XRPD patterns of as prepared samples. Normalized volume $V_n = V/Z$.

Sample	Space group	Unit cell a, b, c (Å)	V (Å^3)	Z	V_n (Å^3)	R_{wp} (%)	R_w (%)	R_{Bragg}	Reduced χ^2
LSFM	R-3c	a = b = 5.5136(2) c = 13.4443(8)	353.55(1)	6	58.99	10.49	6.68	2.07	2.03
LSFMN	R-3c	a = b = 5.4931(2) c = 13.419(1)	350.55(3)	6	58.44	11.52	8.36	4.26	2.30
LSFMC	R-3c	a = b = 5.4972(1) c = 13.4084(3)	350.90(1)	6	58.48	10.56	7.70	4.27	2.83

$m^2 \cdot g^{-1}$). This trend is reflected in a lower pore volume for LSFMC (0.0051 $cm^3 \cdot g^{-1}$), compared to LSFMN (0.0136 $cm^3 \cdot g^{-1}$) and LSFM (0.014 $cm^3 \cdot g^{-1}$) (Fig. S1), further confirming the different morphology and textural properties induced by copper substitution into LSFM.

Thermogravimetric analysis in N_2 atmosphere (N_2-TGA) was carried out to evaluate the effect of Cu and Ni substitutions on the LSFM surface oxygen retention capacity. Looking at Fig. 2m, for all samples the weight loss is lower than 1.5% at 900 °C, ascribed to thermally activated lattice oxygen removal. Up to 900 °C, LSFM and LSFMN display a similar trend, with a slightly higher loss for LSFMN (0.93%) with respect to the undoped LSFM (0.77%). In contrast, LSFMC shows a different behavior characterized by an abrupt change in slope at 280 °C, indicative of a more favorable lattice oxygen depletion, reaching a final weight loss of 1.34%. Interestingly, Fe replacement with Cu, despite leading to a specific surface area decrease, resulted in a higher tendency to form oxygen vacancies as compared to Ni substitution. This behavior already observed in Cu-substituted ferrites [39], is likely to be attributed to a lowered average B-site oxidation state introduced by Cu^{2+}/Cu^{3+} cations, as opposed to Ni^{2+}/Ni^{3+}.

3.2. Structural and morphological analysis of reduced compounds

The structural stability and the morphological evolution of LSFM, LSFMN and LSFMC after reduction for 2 h at 850 °C in 5% H_2/Ar have been assessed. The XRPD patterns of the reduced samples, along with the corresponding Rietveld refinement, are reported in Fig. 3. As shown in Fig. 3a, the ABO_3 perovskite phase shown by all as prepared samples evolves into a Ruddlesden-Popper (RP) structure A_2BO_4, composed of layers of cubic perovskite ($La_{0.6}Sr_{0.4}Fe_{1-x-y}Mn_x(Ni,Cu)_yO_{3-\delta}$) alternating with rock salt layers ($La_{0.6}Sr_{0.4}O_{1+w}$), exhibiting the typical double peaks around 2θ = 32°. Interestingly, other peaks are present in the 2θ region 40°-50°, which can be ascribed to the reduction to the metallic state of B-site Fe, Ni and Cu cations.

The Rietveld refinement plots of the XRPD patterns of LSFM_R, LSFMN_R and LSFMC_R are presented in Fig. 3b, c, d and the corresponding phase compositions are summarized in Table 2. The Rietveld refinement of LSFM_R data (Fig. 3b) reveals a non-complete phase transition: RP-structure of formula $La_{1.2}Sr_{0.8}Fe_{0.85}Mn_{0.15}O_4$ (47.72(4) mol%), metallic Fe^0 (40.46(33) mol%), Fe-free perovskite $La_{0.6}Sr_{0.4}MnO_{3-\delta}$ (7.45(8) mol%), and MnO (4.37(16) mol%) are present. During the treatment, iron and manganese reductions take place

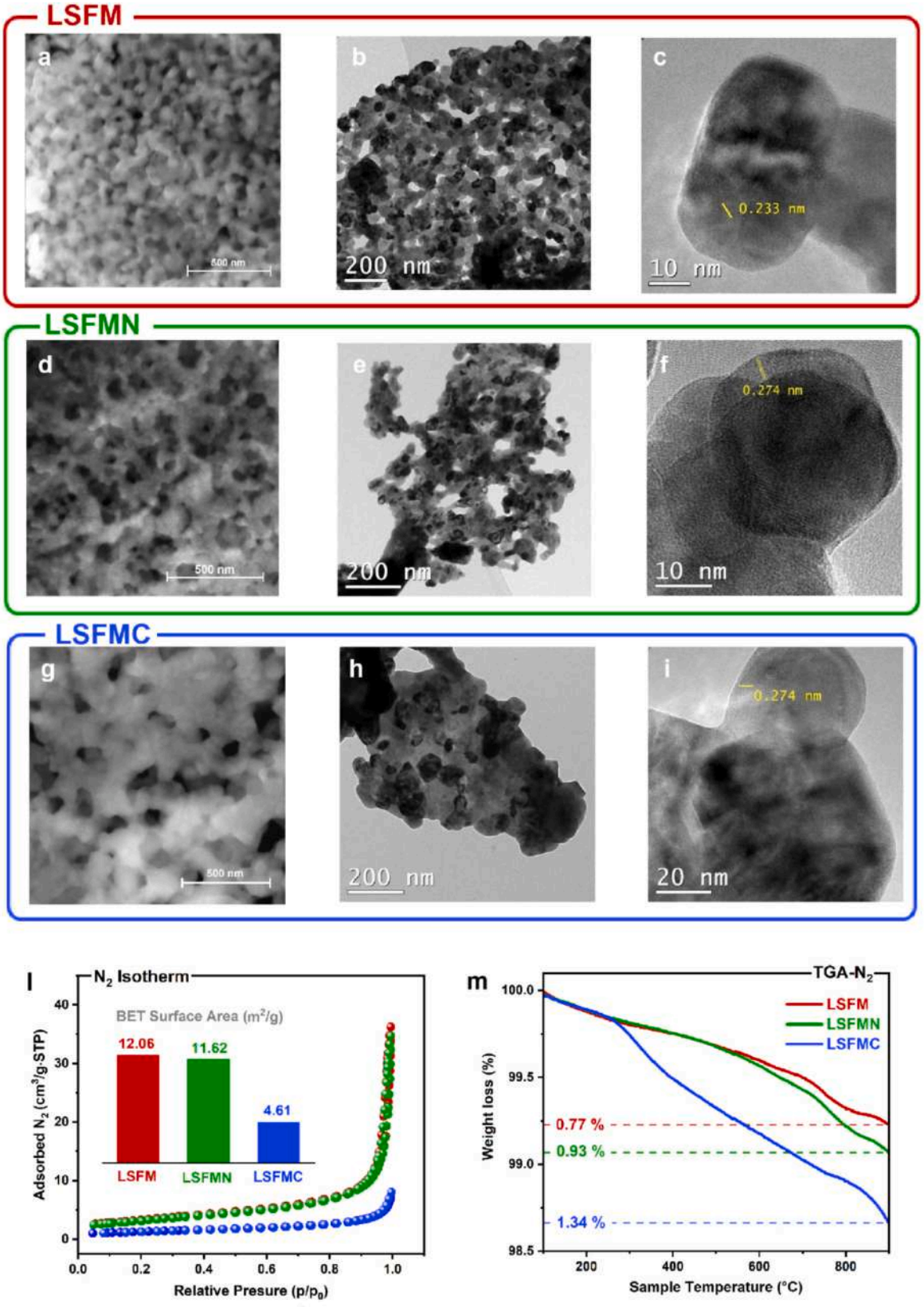

Fig. 2. Morphological characterization of as prepared materials: a) SEM and b-c) TEM analyses of LSFM; d) SEM and e-f) TEM analyses of LSFMN; g) SEM and h-i) TEM analyses of LSFMC. The yellow bars in c), f), i) represent the sample area used to calculate the d-spacing reported in the figure; l) N_2 adsorption/desorption isotherms and BET surface area values and m) N_2-TGA analysis for LSFM, LSFMN and LSFMC samples.

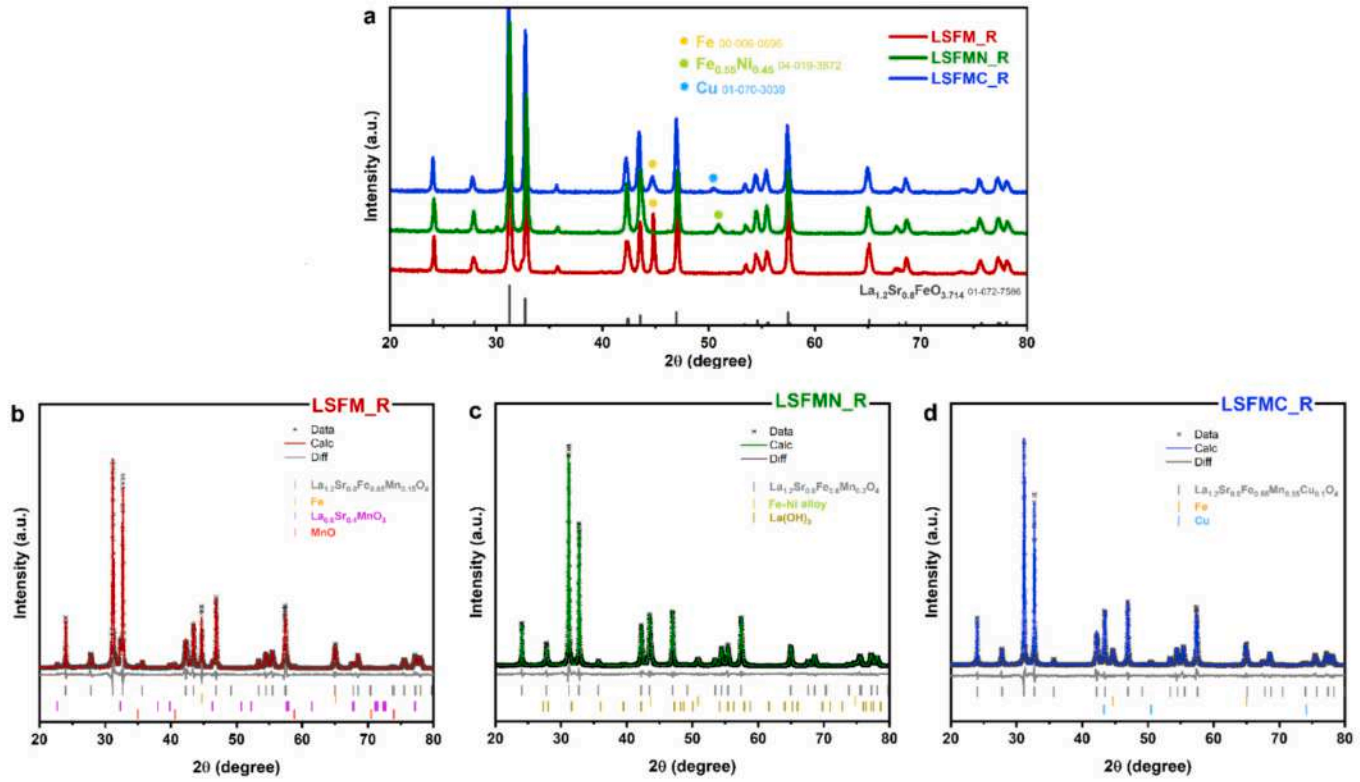

Fig. 3. Structural characterization of materials after 2 h reduction in 5% H_2/Ar at 850 °C. a) XRPD patters comparison of LSFM_R, LSFMN_R and LSFMC_R; Rietveld refinement of b) LSFM_R, c) LSFMN_R and d) LSFMC_R.

Table 2
Phase compositions (mol%) of reduced samples (in 5% H_2/Ar at 850 °C for 2 h) obtained by Rietveld refinements.

Phases		LSFM_R	LSFMN_R	LSFMC_R
$La_{1.2}Sr_{0.8}Fe_{0.85}Mn_{0.15}O_4$		47.72(4)	–	–
Fe (bcc)		40.46(33)	–	31.62(36)
$La_{0.6}Sr_{0.4}MnO_3$		7.45(8)	–	–
MnO		4.37(16)	–	–
$La_{1.2}Sr_{0.8}Fe_{0.6}Mn_{0.4}O_4$		–	52.16(2)	–
Fe-Ni (fcc)		–	46.79(37)	–
$La(OH)_3$		–	1.05(3)	–
$La_{1.2}Sr_{0.8}Fe_{0.55}Mn_{0.35}Cu_{0.1}O_4$		–	–	53.91(2)
Cu (fcc)		–	–	14.47(35)
		R_{Bragg} = 5.64, reduced χ^2 = 3.38	R_{Bragg} = 3.82, reduced χ^2 = 19.5	R_{Bragg} = 3.82, reduced χ^2 = 2.26

but, unlike iron, Mn is not reduced to its metallic state. In accordance with our previous findings [27], MnO is formed as an intermediate compound during the perovskite-to-RP transformation, promoting the structural integrity of the perovskite and thus avoiding the structure break-up as in the case of Mn-free LSF perovskite [40]. The XRPD pattern of LSFMN_R (Fig. 3c) exhibits $La_{1.2}Sr_{0.8}Fe_{0.6}Mn_{0.4}O_4$ RP phase (52.16(2) mol%), Fe—Ni alloy (46.79(37) mol%) and $La(OH)_3$ (1.05(3) mol%). The formation of Fe—Ni alloy nanoparticles on the perovskite surface has been also reported by Ding et al. [41]: co-doping Fe and Ni increases the oxygen vacancy concentration, lowering the segregation energy of Fe down to a value close to that of Ni. The XRD pattern of LSFMC_R (Fig. 3d) shows three phases: $La_{1.2}Sr_{0.8}Fe_{0.55}Mn_{0.35}Cu_{0.1}O_4$ (53.91(2) mol%), metallic Fe^0 (31.62(36) mol%) and metallic Cu^0 (14.47(35) mol%) with co-segregation of iron and copper. Comparing the phase composition of LSFMN_R and LSFMC_R with that of LSFM_R it can be concluded that, after 2 h at 850 °C in 5% H_2/Ar, residual traces of the ABO_3 perovskite phase are detected only in LSFM_R. This observation suggests that the perovskite-to-RP transformation is kinetically favoured by 20 mol% Ni or Cu substitution at LSFM B-site.

The reduced LSFM and LSFMC samples have been studied by SEM/TEM/EDX analyses and summarized in Fig. 4. For LSFM_R, SEM and TEM observations in Figs. 4a, c and S2 reveal a moderately sintered microstructure characterized by partially coalesced nanoparticles with an average particle size of approximately 50–100 nm, significantly larger than in the as prepared sample, in agreement with the applied thermal treatment. No distinct microstructural features attributed to metallic exsolution are visible, yet the EDX mapping in Fig. 4b highlights the presence of segregated iron with particles size exceeding 100 nm, and no evidence of other metallic segregation (Fig. S3). EDX analyses were carried out on different points from *a* to *g*, indicated in Fig. 4d, e and Table S1. High Fe content is identified in spot *g*, exhibiting a Fe concentration of 50.5%. Spots *b*, *c* and *d* are also clearly enriched in iron, indicating metallic iron segregation, whereas spots *a* and *e* have compositions consistent with the RP phase, displaying cation ratios $La_{1.5}Sr_{0.6}Fe_{0.5}Mn_{0.4}$ and $La_{1.5}Sr_{0.4}Fe_{0.5}Mn_{0.5}$ respectively. The composition measured at point *f* appears as intermediate, likely reflecting a contribution from both a metallic iron particle and an underlying RP-phase grain.

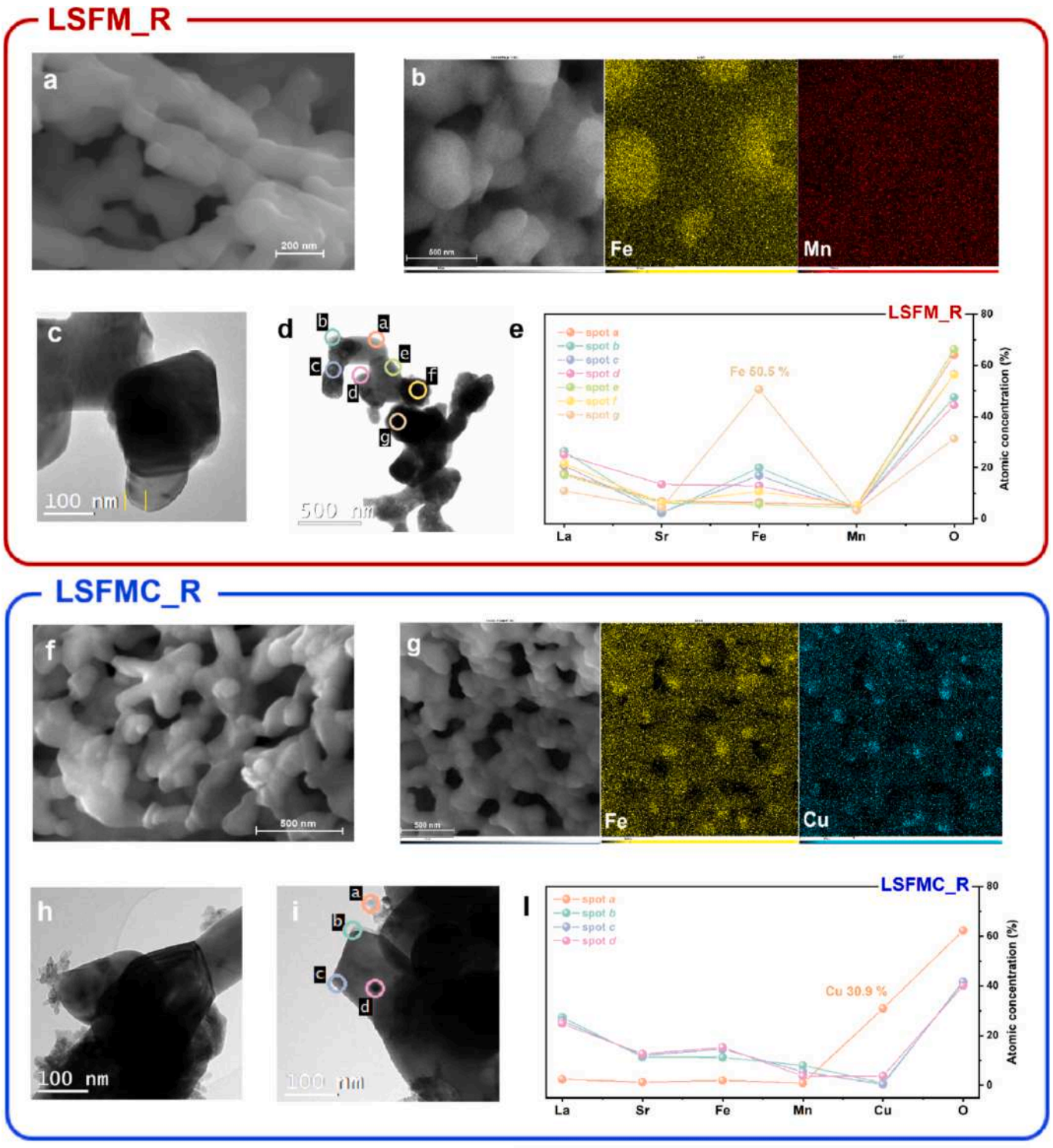

Fig. 4. Morphological characterization of LSFM and LSFMC after 2 h reduction in 5% H_2/Ar at 850 °C. a) SEM analysis, b) EDX mapping, c-d) TEM analysis and e) EDX analysis on different spots for LSFM_R; f) SEM analysis, g) EDX mapping, h-i) TEM analysis and l) EDX analysis on different spots for LSFMC_R.

Similarly to LSFM_R, the SEM/TEM micrographs of LSFMC_R in Figs. 4f and S4a show significant grain coarsening after reduction, with sub-micrometer grains (100–200 nm). EDX mapping in Fig. 4g clearly shows the co-presence of both metallic Cu and Fe segregation, with no detectable compositional variations for the other elements (Fig. S5). The sample surface is covered by low-contrast features (Fig. 4h) forming ramified aggregates with characteristic sizes of approximately ~50–100 nm, which can be attributed to segregated Cu (spot *a* in Fig. 4i, l and Table S2). In analogy with sample LSFM_R, iron particles are not easily identified by morphology, except for few small, high contrast, round nanoparticles (Fig. S4b) with diameters typically around ~10–20 nm. EDX analyses confirms that these particles are Fe-rich (spot *d* in Fig. 4i, l and Table S2). As revealed by XRPD, Fe and Cu segregated particles coexist, suggesting element-specific nucleation and growth during reduction. The elemental composition of the nearby crystals is consistent with the Ruddlesden-Popper phase: spots *b* and *c* in Fig. 4i, l and

Table S2 show cation stoichiometries of $La_{1.40}Sr_{0.58}Fe_{0.58}Mn_{0.41}Cu_{0.04}$ and $La_{1.34}Sr_{0.62}Fe_{0.75}Mn_{0.28}Cu_{0.02}$, respectively, in fair agreement with the composition obtained from Rietveld refinement.

Ni cations at the B-site are known to be easily reduced and exsolved onto the perovskite oxide surface when exposed to a reducing environment at high temperature. To investigate this process, H_2-TPR analysis of LSFMN was performed and presented in Fig. 5a, together with reference samples LSFM and LSF ($La_{0.6}Sr_{0.4}FeO_{3-\delta}$) for comparison. The LSFM sample exhibits two main peaks, one at 320 °C, ascribed to Fe^{4+} ➔ Fe^{3+} reduction, and the second at 390 °C, related to Mn^{4+} ➔ Mn^{3+} transition [27]. A broad feature above 700 °C is observed in all three samples and is ascribable to Fe^{3+} ➔ Fe^{2+}➔ Fe^0 reduction, with a maximum at $T > 900$ °C. The introduction of 20% Ni at the B-site dramatically changes the reduction profile of LSFM. The Fe^{4+} ➔ Fe^{3+} reduction peak shifts to lower temperature (228 °C): likely, further substituting Fe with Ni destabilizes the lattice, leading to an earlier Fe^{4+} reduction [42], while the Mn^{4+} ➔ Mn^{3+} reduction peak overlaps with the more intense Ni^{3+} ➔ $Ni^{2+}$and Ni^{2+} ➔ Ni^0 reductions at 313 °C and 392 °C, respectively [43,44]. Notably, the presence of easily reducible Ni cations facilitates Fe reduction at higher temperature, shifting the Fe^{3+} ➔ Fe^{2+}➔ Fe^0 peak to 757 °C, in accordance to Ding et al.'s work [41] as previously mentioned. After 2 h reduction treatment at 850 °C in 5% H_2/Ar, the TEM micrographs show that LSFMN_R aggregates and particles sizes slightly increased compared to the as-prepared sample (Fig. S6a). As shown in Fig. 5b, c, d metallic nanoparticles are clearly visible across the entire surface of the reduced sample with an average diameter of approximately ~30 nm (Fig. S6b). The EDX mapping analyses in Figs. 5e and S7 confirm the Ni^0-rich nature of the surface exsolved nanoparticles, with no evidence of further segregation. In Fig. 5f, the *d*-spacing measured for the adjacent oxide phase is $d = 0.205$ nm, close to the refined *(111)* plane of the *F-3 m* cubic Fe—Ni alloy (0.207 nm) and the one of the nearby substrates is $d = 0.274$ nm, corresponding to the (*110*) plane for the tetragonal *I4/mmm* Ruddlesden-Popper phase. The TEM/EDX analyses in Fig. 5g, h and Table S3, further confirm an average composition of approximately $Fe_{0.6}Ni_{0.4}$ for the metallic particles (spot *a*), in agreement with the Rietveld refinement of the exsolved phase. The composition of the adjacent phase (spot *b*) is consistent with that of the residual Ruddlesden–Popper structure, with a normalized cation ratio of $La_{1.21}Sr_{0.72}Fe_{0.73}Mn_{0.28}Ni_{0.07}$.

To assess the stability of LSFMN in a $CO:CO_2$ rSOC operating environment, the same reduction treatment was performed in 50:50 $CO:CO_2$ atmosphere, for 2 h at 850 °C. From the XRPD in Fig. S8a, after $CO:CO_2$

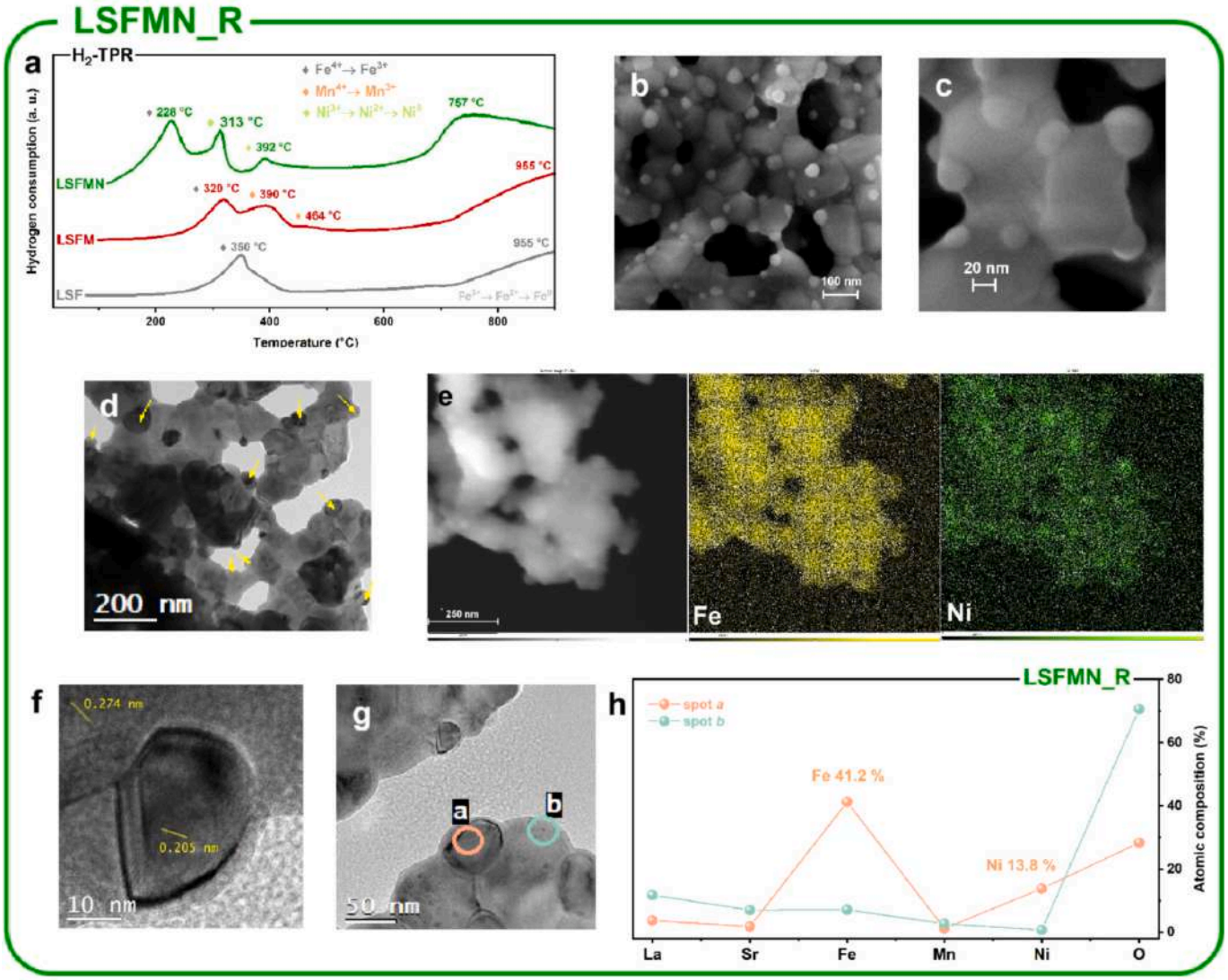

Fig. 5. Morphological characterization of LSFMN_R after 2 h reduction in 5% H_2/Ar at 850 °C. a) H_2-TPR analysis of LSFMN, with LSF and LSFM as references materials; b-c) SEM analysis, d) TEM analysis and e) EDX mapping of LSFMN_R; f-g) TEM analysis of exsolved nanoparticles and h) EDX analysis on different points for LSFMN_R.

exposure the perovskite structure is preserved, with a minor presence of secondary phases. Remarkably, the Fe—Ni alloy peaks are already evident, indicating that a $CO:CO_2$ atmosphere is enough to trigger Fe—Ni nanoparticles exsolution. The SEM micrograph and EDX mapping in Fig. S8b, S8c confirm the presence of catalytically active Ni-based exsolved nanoparticles on the perovskite surface.

3.3. Electrochemical characterization

The air-electrochemical activities of LSFM, LSFMN and LSFMC have been assessed by EIS analysis on LSGM-supported symmetric cells (Fig. 6a). The area-specific resistance (ASR) in the 550–850 °C temperature range is presented in Fig. 6b and the obtained values are listed in Table S4. The reference LSFM sample shows the highest resistance in the whole temperature range, with an activation energy of 1.54 ± 0.02 eV. Both the double-substituted stoichiometries showed improved performance with respect to LSFM, with an activation energy slightly lower for LSFMN compared to LSFMC (1.47 ± 0.02 eV and 1.54 ± 0.02 eV, respectively). At lower temperatures (550 °C) the polarization resistance (R_{pol}) values are 26.3 $\Omega{\cdot}cm^2$ and 24.4 $\Omega{\cdot}cm^2$ for LSFMN and LSFMC respectively (Fig. S9). A more significant difference emerges at higher temperatures, where LSFMC shows superior performance towards oxygen reactions with respect to the Ni-substituted material. As shown by the Nyquist plot in Fig. 6c, at 850 °C both doped samples show a lower polarization resistance compared to LSFM, - 38% and - 51% for LSFMN and LSFMC, respectively. The lowest value is thus achieved with LSFMC, with an R_{pol} of 0.08 $\Omega{\bullet}cm^2$, which is 21% lower than LSFMN and is comparable with other recently reported air electrode materials (Table S5).

To better evaluate the Cu-substitution effect on the air-electrode performance of LSFM, the polarization resistance as a function of oxygen partial pressure (pO_2) was assessed for LSFMN and LSFMC, by means of EIS combined with distribution of relaxation times (DRT) analysis (Fig. S10a, S10b). The DRT plots of LSFMN and LSFMC carried out at 750 °C and different pO_2 are shown in Fig. 6d, e. For both samples, three different processes can be identified in different frequency ranges: a higher frequency process HF ($>10^2$ Hz), a medium frequency process MF (10^1–10^2 Hz) and a lower frequency process LF ($<10^0$ Hz). For both samples the HF peak is essentially insensitive to pO_2 variations, retaining the same frequency for all acquired spectra. This process can be attributed to oxygen exchange at the electrode/electrolyte interface, which is largely pO_2 independent and is expected to be similar for samples with the same cell architecture [10]. In contrast, MF and LF peaks exhibit a clear frequency dependency on pO_2 and can be related to oxygen processes inside the electrode [45,46]. As evidenced by the histograms in Fig. S11, the LSFMC samples show lower total R_{pol} with respect to LSFMN in the whole pO_2 range. Since the rate determining step for both samples is related to MF processes, the relation between the MF peak resistance and pO_2 has been investigated using the following equation [47]:

$$R_{MF}^{-1} \propto k \cdot pO_2^n$$

in which k is a pO_2 independent constant and n is a value related to the oxygen processes involved. In the MF range (10^1–10^2 Hz), n value close to 0.5 is typically associated with the molecular oxygen exchange contribution at the electrode surface [48]. While LSFMN exhibits an n value of 0.65, the results shown in Fig. 6f display how the Cu incorporation into LSFM electrode leads to a decrease in the n value down to 0.45, highlighting a more efficient oxygen surface interaction. This improvement results from a larger extent of surface oxygen vacancies in LSFMC, as already observed in TGA results, leading to a better oxygen exchange reaction at the electrode, thus a reduced R_{pol}.

The effect of Ni-substitution on the fuel-electrode performance of LSFM has been evaluated by recording EIS spectra of LSFM and LSFMN

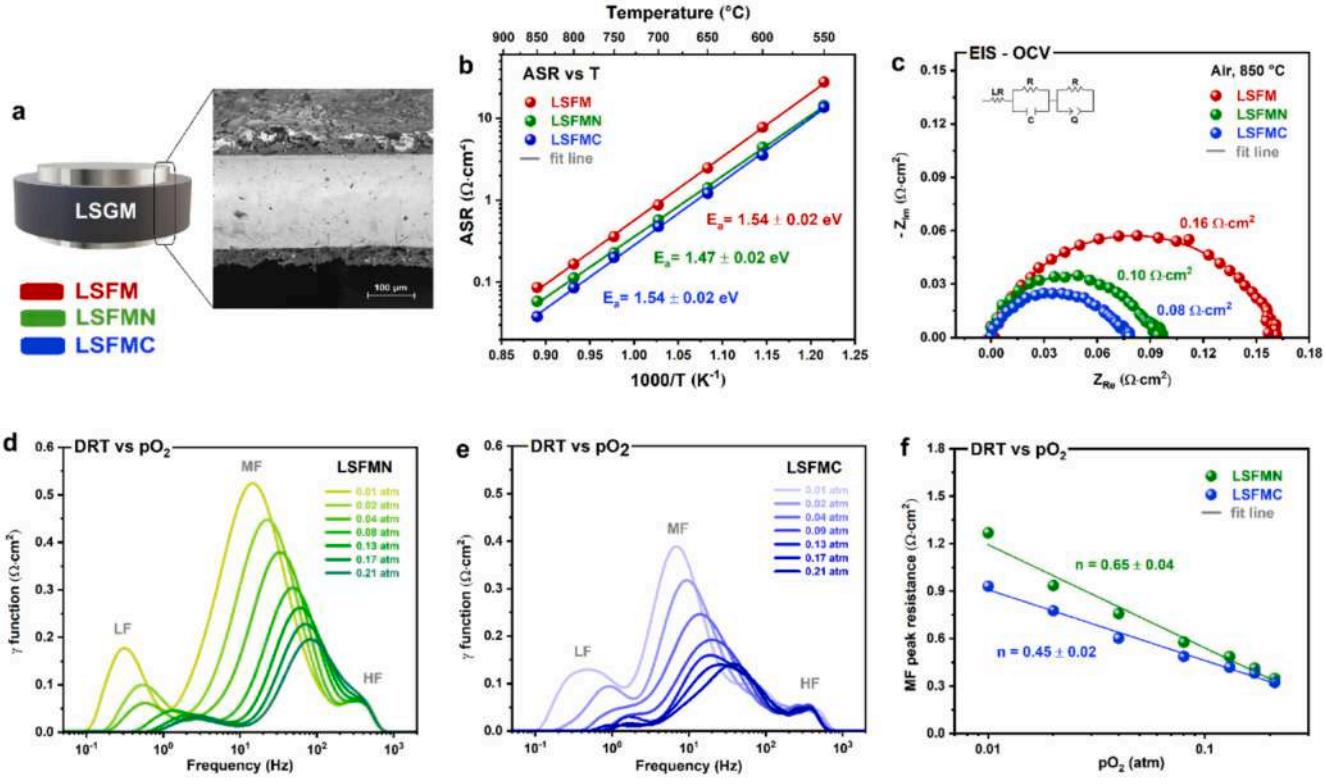

Fig. 6. Air electrode characterization of materials. a) Scheme of cells architecture used for EIS analysis; b) ASR vs T plot at fixed pO_2 of 0.21 atm for LSFM, LSFMN and LSFMC; c) Nyquist plot at 850 °C of LSFM, LSFMN and LSFMC; d-e) DRT plots at 750 °C of LSFMN and LSFMC vs pO_2, respectively; f) R vs pO_2 plot of MF peaks for LSFMN and LSFMC.

symmetric cells in a 50:50 CO:CO_2 atmosphere at open circuit voltage and in a 100% CO_2 atmosphere both at OCV and under a 1.2 V DC bias. Nyquist plots and related DRT analyses are shown in Fig. S12. In 50:50 CO:CO_2 the whole impedance spectrum of the LSFMN-based cell is shifted to higher frequencies and shows a markedly less resistive gas conversion step if compared to the LSFM-based cell (Fig. S12a, S12b). When the cells are tested in 100% CO_2 at OCV (Fig. S12b-c) no CO_2 reduction occurs and the measured OER/ORR polarization resistances are significantly higher than those measured in flowing air (Fig. 6c), due to the lower pO_2 in 100% CO_2. As already observed in Fig. 6c, the LSFMN symmetric cell shows lower impedance compared to LSFM, ascribable to the larger extent of lattice oxygen vacancies of LSFMN. Finally, in 100% CO_2 and under a 1.2 V DC bias, the polarization resistance decreases, as CO_2RR is likely occurring at one of the

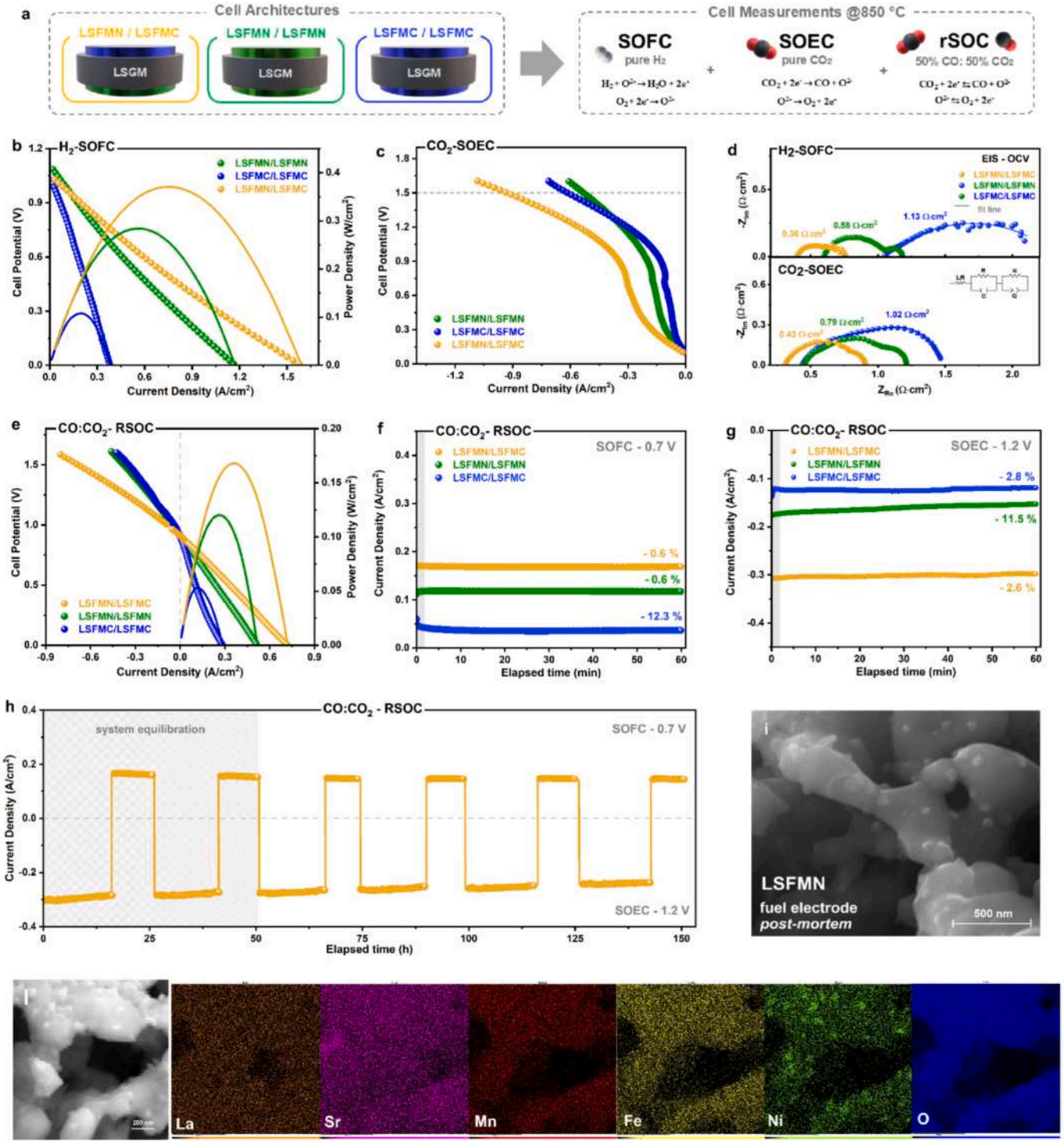

Fig. 7. Cell Tests: a) Scheme of cells architectures (LSFMN/LSFMC, LSFMN/LSFMN, LSFMC/LSFMC) and electrochemical testing carried out at 850 °C in different operational modes and gas-inlet compositions (H_2-SOFC, CO_2-SOEC, CO:CO_2 rSOC); I-V characteristics of the different cells as b) H_2-SOFC and c) CO_2-SOEC; d) Nyquist plot at OCV in H_2 and CO_2; e) I-V characteristics of the different cells as CO:CO_2 reversible SOC and short stability test in f) SOFC mode and g) SOEC mode; h) long-term reversible stability in CO:CO_2 for semi-symmetric LSFMN/LSFMC cell up to 150 h; i) SEM and l) EDX *post-mortem* analysis of spent LSFMN fuel electrode after long-term stability test.

electrodes: as expected, the gas conversion impedance contribution in Fig. S12e, S12f is significantly reduced compared to that measured at open circuit. LSFMN spectrum in Fig. S12f shows a substantial reduction of the MF and LF peaks as compared to those of LSFM, indicating that Ni-substitution effectively enhances LSFM activity towards CO_2RR, combining an increased extent of lattice oxygen vacancies to the presence of Fe—Ni exsolved nanoparticles.

3.4. Cell tests

A schematic representation for all the complete cell architectures along with the electrochemical evaluation has been provided in Fig. 7a. Based on previously presented results, an LSGM-based semi-symmetric cell was fabricated, with LSFMC electrode at the air side and LSFMN electrode at the fuel side (LSFMN/LSFMC, yellow in Fig. 7a). For comparison, the LSFMN/LSFMN and LSFMC/LSFMC symmetric cells have also been prepared (green and blue, respectively in Fig. 7a). All the cells have been tested at 850 °C following the same routine: first as SOFC in pure H_2, then as SOEC in pure CO_2 and finally as reversible SOC in 50:50 CO:CO_2 gas mixture.

The I-V and power density curves in SOFC and SOEC modes at 850 °C are shown in Fig. 7b, c. Focusing first on SOFC operation (Fig. 7b) in pure H_2, the semi-symmetric LSFMN/LSFMC cell presents the best performance compared to symmetric cells, with a maximum power density (MPD) of 371 mW·cm^{-2}. This value is significantly higher than those measured for the symmetric LSFMN/LSFMN cell (284 mW·cm^{-2}) and LSFMC/LSFMC cell (108 mW·cm^{-2}). From the Nyquist plots recorded at open circuit voltage (OCV) (Fig. 7d), the semi-symmetric LSFMN/LSFMC cell has the lowest total polarization resistance (0.36 Ω·cm^2), followed by LSFMN/LSFMN cell (0.58 Ω·cm^2) and LSFMC/LSFMC cell (1.13 Ω·cm^2).

The cells have been tested as SOEC in pure CO_2 and the results at 850 °C are presented in Fig. 7c. The two symmetric cells LSFMN/LSFMN and LSFMC/LSFMC present a similar behavior, with a more resistive trend in the 0.1 V-0.9 V range, below the required overvoltage for CO_2 reduction. A small current contribution is observed at 0.7 V for the LSFMC/LSFMC I-V characteristic, already observed when a Cu-substituted lanthanum strontium ferrite was used as fuel electrode and ascribed to the reduction of surface adsorbed carbonates [39]. The semi-symmetric LSFMN/LSFMC cell presents the best performance, reaching a current density of −0.94 A·cm^{-2} at 1.5 V, higher compared to LSFMN/LSFMN (−0.53 A·cm^{-2}) and LSFMC/LSFMC (−0.60 A·cm^{-2}), with an improvement of polarization resistance by 46% and 58% with respect to LSFMN/LSFMN and LSFMC/LSFMC, respectively (Fig. 7d).

Finally, the cells were tested as reversible SOCs in a 50:50 CO:CO_2 gas mixture, and the resulting I-V and power density curves are presented in Fig. 7e. As expected, the semi-symmetric LSFMN/LSFMC cell exhibits the best results, achieving a MPD of 168 mW·cm^{-2} in SOFC mode and a current density of −0.69 A·cm^{-2} at 1.5 V in SOEC mode, followed by an improvement of polarization resistance at OCV by 26% and 75% compared to LSFMN/LSFMN and LSFMC/LSFMC, respectively (Fig. S13a). Short-term stability tests carried out on the cells (Fig. 7f, g) highlight the semi-symmetric LSFMN/LSFMC cell as the most stable after 1 h in both SOFC mode (0.7 V) and SOEC mode (1.2 V), with a current density loss of −0.6% in SOFC mode and −2.6% in SOEC mode, lower compared to those observed for the other two cell architectures. These electrochemical results confirm that the combination of the high catalytic activity of exsolved Ni-based nanoparticles at the fuel side and the enhanced oxygen reactions activity introduced by Cu-substitution at the air side is a promising strategy to improve cell performance. The semi-symmetric LSFMN/LSFMC cell was therefore selected for cell endurance test as reversible SOC. A long-term reversible stability test was carried out in a 50:50 CO:CO_2 gas mixture and presented in Fig. 7h. The current density was monitored during several SOFC/SOEC cycles at different voltages (0.7 V and 1.2 V, respectively) for up to 150 h operation. Most of the current density loss occurred during the first two cycles and can be attributed to initial system equilibration. After that, the device shows remarkable stability and reversibility for further 100 h. The Nyquist plot recorded at OCV (Fig. S13b) shows that after 150 h the ohmic resistance increased by 25%, likely due to electrolyte degradation. The final total cell polarization resistance (R_{pol}) increased by 42%. Considering that R_{pol} represents the combination of the air electrode and fuel electrode and that it is also negatively affected by the electrolyte degradation, such increase after 150 h can be considered as limited.

After test, LSFMC and LSFMN spent electrodes were retrieved from three identical LSFMN/LSFMC tested cells and characterized via XRPD (Fig. S14a and S14b for LSFMC and LSFMN, respectively). As expected, both electrode materials show remarkable stability, with LSFMC and LSFMN patterns being coherent with those reported in Figs. 1d and S8, respectively. To assess morphological stability after operation, a *post-mortem* SEM-EDX analysis of the cell has been performed. From the micrograph of spent LSFMN fuel electrode in Figs. 7i and S15a, the perovskite surface results still covered by clearly visible and non-coarsened nanoparticles with an average dimension <100 nm. EDX analyses in Figs. 7l and S15b confirm the Fe—Ni composition of these nanoparticles, with no detectable change in the surrounding cation distribution.

4. Conclusions

A rational electrode design strategy for reversible solid oxide cells based on exsolution-enabled Mn-stabilized ferrite perovskites is herein demonstrated. The B-site–substituted compositions $La_{0.6}Sr_{0.4}Fe_{0.6}Mn_{0.2}Ni_{0.2}O_{3-\delta}$ (LSFMN) and $La_{0.6}Sr_{0.4}Fe_{0.6}Mn_{0.2}Cu_{0.2}O_{3-\delta}$ (LSFMC) were synthesized as single-phase materials and exhibit markedly enhanced electrochemical performance compared to the undoped LSFM ferrite.

When employed as oxygen electrodes in symmetric cells, LSFMN and LSFMC reduce the area-specific resistance by approximately 38% and 51%, respectively. Under reducing conditions, LSFMN undergoes controlled in situ exsolution of uniformly distributed Fe—Ni nanoparticles, generating strongly anchored metallic active sites while preserving the integrity of the oxide framework. The exsolution process contributes to the enhanced catalytic activity and redox stability of the fuel electrode, enabling efficient CO oxidation and CO_2 electrolysis under large oxygen partial pressure fluctuations. In contrast, LSFMC exhibits superior oxygen surface exchange and transport properties, making it particularly effective as an air electrode for ORR/OER.

A quasi-symmetric LSGM-supported cell employing LSFMN at the fuel electrode and LSFMC at the air electrode delivers high performance and stable operation in both CO-SOFC and CO_2-SOEC modes, maintaining reversibility for over 150 h without detectable degradation.

Overall, exsolution-engineered Mn-stabilized ferrites are established as a robust, cobalt-free electrode platform for rSOCs, highlighting metal exsolution as a powerful tool to simultaneously achieve high catalytic activity, redox resilience, and long-term durability in reversible CO:CO_2 electrochemical conversion.

CRediT authorship contribution statement

Anna Paola Panunzi: Writing – original draft, Visualization, Software, Methodology, Investigation, Data curation, Conceptualization. **Leonardo Duranti:** Writing – review & editing, Writing – original draft, Validation, Supervision, Methodology, Conceptualization. **Isabella Natali Sora:** Writing – review & editing, Writing – original draft, Software, Methodology, Investigation, Formal analysis. **Renato Pelosato:** Writing – original draft, Software, Investigation, Formal analysis. **Benedetta Bertolotti:** Formal analysis. **Umberto Pasqual Laverdura:** Writing – review & editing, Formal analysis. **Maria Luisa Grilli:** Supervision, Formal analysis. **Elisabetta Di Bartolomeo:** Writing – review & editing, Validation, Supervision, Resources, Project administration, Funding acquisition.

Declaration of competing interest

The authors declare that they have no known competing financial interests or personal relationships that could have appeared to influence the work reported in this paper.

Acknowledgments

This work was funded by the European Union- Next Generation EU, Mission 4, Component 2, CUP E53D2300537 and CUP F53D23002570006, PRIN-2022 project – Prot. 2022ZWYSKY "Advanced materials for reversible solid oxide cells (AMARILLO)".

The authors gratefully acknowledge Nicola Rotiroti for his valuable technical assistance with TEM measurements. TEM analyses were performed at the TEM facility of the Unitech COSPECT at the University of Milan (Italy).

Appendix A. Supplementary data

Supplementary data to this article can be found online at https://doi.org/10.1016/j.cej.2026.175423.

Data availability

Data will be made available on request.

References

[1] A. Hauch, R. Küngas, P. Blennow, A.B. Hansen, J.B. Hansen, B.V. Mathiesen, M. B. Mogensen, Recent advances in solid oxide cell technology for electrolysis, Science 370 (2020) eaba6118.
[2] R. Küngas, P. Blennow, T. Heiredal-Clausen, T. Holt, J. Rass-Hansen, S. Primdahl, J.B. Hansen, eCOs-a commercial CO_2 electrolysis system developed by Haldor Topsoe, ECS Trans. 78 (2017) 2879.
[3] J. Liang, M. Han, Different performance and mechanisms of CO_2 electrolysis with CO and H_2 as protective gases in solid oxide electrolysis cell, Int. J. Hydrog. Energy 47 (2022) 18606–18618.
[4] W. Zhang, Y.H. Hu, Material design and performance of carbon monoxide-fueled solid oxide fuel cells: a review, Energy Sci. Eng. 11 (2023) 3276–3288.
[5] M.B. Mogensen, Materials for reversible solid oxide cells, Curr. Opin. Electrochem. 21 (2020) 265–273.
[6] L. Fang, F. Liu, H. Ding, C. Duan, High-performance reversible solid oxide cells for powering electric vehicles, long-term energy storage, and CO_2 conversion, ACS Appl. Mater. Interfaces 16 (2024) 20419–20429.
[7] J. Jung, S.W. Lee, J. Lee, G. Lee, J.H. Joo, T.H. Shin, S. Kang, Decarbonizing cement production via tail-end integration of solid oxide electrolysis for CO_2 reduction, Chem. Eng. J. 520 (2025) 166281.
[8] J.-W. Park, H.-B. Park, K.-T. Lee, Direct Linz-Donawitz converter gas fueled solid oxide fuel cells, J. Power Sources 658 (2025) 238267.
[9] S. Higashidani, H. Watanabe, Enhancement of Ni oxidation tolerance in Ni/GDC cathode surface during CO_2/H_2O electrolysis in SOEC, Int. J. Hydrog. Energy 155 (2025) 150319.
[10] A.P. Panunzi, L. Duranti, I. Luisetto, N. Lisi, M. Marelli, E. Di Bartolomeo, Triggering electrode multi-catalytic activity for reversible symmetric solid oxide cells by Pt-doping lanthanum strontium ferrite, Chem. Eng. J. 471 (2023) 144448.
[11] A.P. Panunzi, L. Duranti, U. Draz, S. Licoccia, C. D'Ottavi, E. Di Bartolomeo, Improved surface activity of lanthanum ferrite perovskite oxide through controlled Pt-doping for solid oxide cell (SOC) electrodes, Ceram. Int. 50 (2024) 31442–31450.
[12] M. Marasi, L. Duranti, I. Luisetto, E. Fabbri, S. Licoccia, E. Di Bartolomeo, Ru-doped lanthanum ferrite as a stable and versatile electrode for reversible symmetric solid oxide cells (r-SSOCs), J. Power Sources 555 (2023) 232399.
[13] C. Yuan, D. Feng, H. Ye, P. Shan, L. Ge, H. Chen, Y. Zheng, S. Cui, B-site high valence cation co-doping boosts fast oxygen kinetics in a cobalt-free perovskite air electrode for reversible solid oxide cells, J. Mater. Chem. A 13 (2025) 32562–32576.
[14] X. Han, Y. Ling, Y. Yang, Y. Wu, Y. Gao, B. Wei, Z. Lv, Utilizing high entropy effects for developing chromium-tolerance cobalt-free cathode for solid oxide fuel cells, Adv. Funct. Mater. 33 (2023) 2304728.
[15] D.Z. De Florio, R. Muccillo, V. Esposito, E. Di Bartolomeo, E. Traversa, Preparation and electrochemical characterization of perovskite/YSZ ceramic films, J. Electrochem. Soc. 152 (2004) A88.
[16] S. Biswas, D.S. Dhawale, T. Hosseini, G. Kaur, S. Giddey, N. Haque, A review on critical metals used in solid oxide cells for power ↔ X applications and materials recyclability, ACS Sustain. Chem. Eng. 12 (2024) 6037–6058.
[17] G. Ragonnaud, Critical Raw Materials Act, EPRS, Bruxelles, Belgium, European Parliament, 2023.
[18] S.P. Simner, J.F. Bonnett, N.L. Canfield, K.D. Meinhardt, J.P. Shelton, V. L. Sprenkle, J.W. Stevenson, Development of lanthanum ferrite SOFC cathodes, J. Power Sources 113 (2003) 1–10.
[19] S. Sen, M. Palabathuni, K.M. Ryan, S. Singh, High entropy oxides: mapping the landscape from fundamentals to future vistas: focus review, ACS Energy Lett. 9 (2024) 3694–3718.
[20] W. Zhang, W. Ma, Y. Gao, X. Han, F. Jin, L. Zhao, K. Zheng, Y. Ling, P. Feng, S. Wang, Small-size atom-driven distortion realizes high-entropy oxides with simultaneous chemical stability and activity enhancement enabling a practical cathode for solid oxide fuel cells, Appl. Catal. B Environ. Energy 383 (2025) 126147.
[21] J. Dąbrowa, A. Olszewska, A. Falkenstein, C. Schwab, M. Szymczak, M. Zajusz, M. Moździerz, A. Mikuła, K. Zielińska, K. Berent, An innovative approach to design SOFC air electrode materials: high entropy $La_{1-x}Sr_x(Co, Cr, Fe, Mn, Ni)O_{3-\delta}$ (x= 0, 0.1, 0.2, 0.3) perovskites synthesized by the sol–gel method, J. Mater. Chem. A 8 (2020) 24455–24468.
[22] Z. Liu, Z. Zhou, J. Yang, Y. Sun, C. Yin, R. Li, K. Wu, A. Chatzitakis, J. Zhou, Design of a B-site co-free multielement perovskite oxide as oxygen electrode for efficient CO_2 solid oxide electrolysis cells, ACS Appl. Energy Mater. 7 (2024) 11020–11030.
[23] X. Li, T. Chen, C. Wang, N. Sun, G. Zhang, Y. Zhou, M. Wang, J. Zhu, L. Xu, S. Wang, An active and stable high-entropy Ruddlesden-Popper type $La_{1.4}Sr_{0.6}Co_{0.2}Fe_{0.2}Ni_{0.2}Mn_{0.2}Cu_{0.2}O_{4\pm\delta}$ oxygen electrode for reversible solid oxide cells, Adv. Funct. Mater. 34 (2024) 2411216.
[24] R. Li, J. Zhang, Z. Chen, X. Qian, Y. Gao, F. Jin, D.S. Tsvetkov, Y. Ling, A stable high-entropy perovskite $La_{0.2}Pr_{0.2}Nd_{0.2}Sm_{0.2}Sr_{0.2}Co_{0.8}Fe_{0.2}O_{3-\delta}$ oxygen electrode for reversible solid oxide cells, Mater. Sci. Eng. B Solid-State Mater. Adv. Technol. 313 (2025) 117857.
[25] T. Götsch, L. Schlicker, M.F. Bekheet, A. Doran, M. Grünbacher, C. Praty, M. Tada, H. Matsui, N. Ishiguro, A. Gurlo, Structural investigations of $La_{0.6}Sr_{0.4}FeO_{3-\delta}$ under reducing conditions: kinetic and thermodynamic limitations for phase transformations and iron exsolution phenomena, RSC Adv. 8 (2018) 3120–3131.
[26] T. Götsch, N. Köpfle, L. Schlicker, E.A. Carbonio, M. Hävecker, A. Knop-Gericke, R. Schloegl, M.F. Bekheet, A. Gurlo, A. Doran, Treading in the limited stability regime of lanthanum strontium ferrite—reduction, phase change and exsolution, ECS Trans. 91 (2019) 1771.
[27] L. Duranti, I.N. Sora, F. Zurlo, I. Luisetto, S. Licoccia, E. Di Bartolomeo, The role of manganese substitution on the redox behavior of $La_{0.6}Sr_{0.4}Fe_{0.8}Mn_{0.2}O_{3-\delta}$, J. Eur. Ceram. Soc. 40 (2020) 4076–4083.
[28] Y.S. Chung, T. Kim, T.H. Shin, H. Yoon, S. Park, N.M. Sammes, W.B. Kim, J. S. Chung, In situ preparation of a La1.2Sr0.8Mn0.4Fe0.6O4 ruddlesden–popper phase with exsolved Fe nanoparticles as an anode for SOFCs, J. Mater. Chem. A 5 (2017) 6437–6446.
[29] L. Duranti, I. Luisetto, S. Licoccia, C. Del Gaudio, E. Di Bartolomeo, Electrochemical performance and stability of LSFMn+ NiSDC anode in dry methane, Electrochim. Acta 362 (2020) 137116.
[30] K.-T. Wu, T. Ishihara, Superior syngas product control of La(Sr)Fe(Mn)O_3 perovskite in high-temperature CO_2/H_2O co-electrolysis, Appl. Catal. B Environ. Energy 357 (2024) 124335.
[31] T. Ishihara, S. Wang, K.-T. Wu, Highly active oxide cathode of La(Sr)Fe(Mn)O_3 for intermediate temperature CO_2 and CO_2-H_2O co-electrolysis using LSGM electrolyte, Solid State Ionics 299 (2017) 60–63.
[32] S.W. Lee, T.H. Nam, M. Kim, S. Lee, K.H. Lee, J.H. Park, T.H. Shin, Enhancing CO 2 electrolysis performance with various metal additives (Co, Fe, Ni, and Ru)–decorating the La (Sr) Fe (Mn) O $_3$ cathode in solid oxide electrolysis cells, Inorg. Chem. Front. 10 (2023) 3536–3543.
[33] S. Wang, H. Tsuruta, M. Asanuma, T. Ishihara, Ni–Fe–La (Sr) Fe (Mn) O_3 as a new active cermet cathode for intermediate-temperature CO_2 electrolysis using a $LaGaO_3$-based electrolyte, Adv. Energy Mater. 5 (2015) 1401003.
[34] K.-T. Wu, T. Ishihara, Designing highly active electrode by infiltration technique for co-electrolysis of CO_2 and H_2O, Solid State Ionics 425 (2025) 116867.
[35] Z. Heng, Y. Wan, C. Xia, Calcium stabilized $La_{0.6}Sr_{0.4}Fe_{0.8}Mn_{0.2}O_{3-\delta}$ perovskite as ceramic fuel electrode for solid oxide cell, J. Power Sources 537 (2022) 231535.
[36] A.C. Larson, R.B. Von Dreele, General Structure Analysis System (GSAS), Los Alamos National Laboratory Report LAUR, 2000, pp. 86–748.
[37] T.H. Wan, M. Saccoccio, C. Chen, F. Ciucci, Influence of the discretization methods on the distribution of relaxation times deconvolution: implementing radial basis functions with DRTtools, Electrochim. Acta 184 (2015) 483–499.
[38] S. Dann, D. Currie, M. Weller, M. Thomas, A. Al-Rawwas, The effect of oxygen stoichiometry on phase relations and structure in the system $La_{1-x}Sr_xFeO_{3-\delta}$ ($0 \le x \le 1$, $0 \le \delta \le 0.5$), J. Solid State Chem. 109 (1994) 134–144.
[39] U. Draz, E. Di Bartolomeo, A.P. Panunzi, U. Pasqual Laverdura, N. Lisi, R. Chierchia, L. Duranti, Copper-enhanced CO_2 electroreduction in SOECs, ACS Appl. Mater. Interfaces 16 (2024) 8842–8852.
[40] X. Liu, D. Han, Y. Zhou, X. Meng, H. Wu, J. Li, F. Zeng, Z. Zhan, Sc-substituted $La_{0.6}Sr_{0.4}FeO_{3-\delta}$ mixed conducting oxides as promising electrodes for symmetrical solid oxide fuel cells, J. Power Sources 246 (2014) 457–463.
[41] S. Ding, M. Li, W. Pang, B. Hua, N. Duan, Y.-Q. Zhang, S.-N. Zhang, Z. Jin, J.-L. Luo, A-site deficient perovskite with nano-socketed Ni-Fe alloy particles as highly active and durable catalyst for high-temperature CO_2 electrolysis, Electrochim. Acta 335 (2020) 135683.
[42] S.M. Alizadeh, P. Roussel, M. Golmohammad, V. Theuns, D. Fagg, O.I. Lebedev, E. Berrier, Y.V. Kolen'Ko, Investigating reduction and oxidation of $La_{0.72}Sr_{0.18}Fe_{0.9}Ni_{0.1}O_{3-\delta}$ as a Co-free perovskite electrode for symmetrical solid oxide cells, J. Phys. Energy 7 (2025) 035010.
[43] X. Wang, H. Wang, L. Hu, B. Ge, L. Guo, Z. Yang, Highly CO_2RR activity and electrochemical performance of A-site deficient symmetrical electrode materials

$(La_{0.6}Sr_{0.4})_{1-x}Fe_{0.8}Ni_{0.2}O_{3-\delta}$ for CO_2 electrolysis, J. Eur. Ceram. Soc. 43 (2023) 6974–6981.

[44] J. Kim, M. Ferree, S. Gunduz, J.-M.M. Millet, M. Aouine, U.S. Ozkan, Exsolution of nanoparticles on A-site-deficient lanthanum ferrite perovskites: its effect on co-electrolysis of CO_2 and H_2O, J. Mater. Chem. A 10 (2022) 2483–2495.

[45] J.-D. Kim, G.-D. Kim, J.-W. Moon, Y.-i. Park, W.-H. Lee, K. Kobayashi, M. Nagai, C.-E. Kim, Characterization of LSM–YSZ composite electrode by ac impedance spectroscopy, Solid State Ionics 143 (2001) 379–389.

[46] M. Escudero, A. Aguadero, J.A. Alonso, L. Daza, A kinetic study of oxygen reduction reaction on La_2NiO_4 cathodes by means of impedance spectroscopy, J. Electroanal. Chem. 611 (2007) 107–116.

[47] Y. Takeda, R. Kanno, M. Noda, Y. Tomida, O. Yamamoto, Cathodic polarization phenomena of perovskite oxide electrodes with stabilized zirconia, J. Electrochem. Soc. 134 (1987) 2656.

[48] L. Shen, Z. Du, Y. Zhang, X. Dong, H. Zhao, Medium-entropy perovskites Sr$(Fe_\alpha Ti_\beta Co_\gamma Mn_\zeta)$ $O_{3-\delta}$ as promising cathodes for intermediate temperature solid oxide fuel cell, Appl. Catal. B Environ. 295 (2021) 120264.